Saturation of shape instabilities in single-bubble sonoluminescence

Mogens T. Levinsen*
Niels Bohr Institute, University of Copenhagen, Copenhagen, Denmark
(Received 9 May 2014; published 29 July 2014)

Excitation of shape instabilities represents one route to bubble death in single-bubble sonoluminescence. This feature is satisfactorily explained by an expansion to first order in the amplitude of a shape distortion in the form of a spherical harmonic. By taking the expansion to second order, it is found that regions of parameter space exist where the exponential growth into bubble disruption is checked and a saturated stable state of shape distortion is possible. Experimental evidence provided by Mie scattering is presented, and a possible connection to simultaneous spatially anisotropic light emission is discussed.

DOI: 10.1103/PhysRevE.90.013026 PACS number(s): 78.60.Mq, 44.40.+a, 52.35.Tc

I. INTRODUCTION

In single bubble sonoluminescence (SBSL) [1] a bubble is held in space by a resonant ultrasound pincer and brought to oscillate at its frequency. If the field is sufficiently strong, adiabatic heating caused by violent bubble collapse leads to elevated temperatures resulting in light emission. The details of the spherical vibrations of the bubble are well described by theory (for reviews see, e.g., Refs. [2,3]). What is not well understood is the reason behind the spatial anisotropy and even period doubling of the emission encountered at some parameter values, although even from the first observations these phenomena were believed to be due to the excitation of shape distortion [4–7]. That the excitation of shape instabilities leads to bubble death has long been accepted since theoretical predictions of the boundary line for excitation coincide well with experimental observation of bubble extinction [8–10]. However, only recently has Mie scattering [11] provided direct observations of instabilities in the SBSL regime [12]. Furthermore, exactly which type of instability is actively engaged in bubble death in the different parameter regimes has not yet been determined experimentally. The recent Mie scattering measurements showed the existence in regions of parameter space of what seems to be long-time stable shape oscillations. In the same regions stable spatially anisotropic period doubling of the emission is found. The two phenomena always seem to occur together. However, according to present first order theory the shape distortion either leads to bubble death or disappears again when excited. In the following an extension of the theory will be presented that shows the existence of islands of saturation of the amplitude of the shape distortion in accordance with the experimental findings. While of foremost interest for SBSL, the result may also be of interest in the field of encapsulated bubbles used for medical purposes (see, e.g., Refs. [13–15]) as well as in inertial confinement fusion (see, e.g., Ref. [16]).

II. BACKGROUND

So far the theory developed is a first order expansion in the disturbance that is assumed to be described by a spherical harmonic with a time-dependent amplitude $a_n(t)$ so that the distorted surface is given by

$$r_s(t) = R(t) + a_n(t) Y_n^m(\theta,\phi), \tag{1}$$

where $R(t)$ is the radius of the bubble in the perfect spherical shape, and $m = 0$ is chosen in accord with measurements on large bubbles.

By assuming that the velocity field around the bubble could be derived from a potential, Plesset [17] derived an amplitude equation for the disturbance to first order in $a_n(t)$; however, effects of viscosity were neglected. The derivation was later extended by Prosperetti [18], who included the influence of viscosity, which due to the integro-differential nature is much more difficult to treat.

Collecting terms of zero order in $a_n(t)$ the derivation by Plesset results in the well-known Rayleigh-Plesset equation where the viscosity of the gas has been neglected since $\mu_1 \ll \mu_2$:

$$R(t)\ddot{R}(t) + \frac{3}{2}\dot{R}(t)^2 = \frac{1}{(\rho_2 - \rho_1)} \times \left[P_1 - P_2 - \frac{2\sigma}{R(t)} - \frac{4\mu_2 \dot{R}(t)}{R(t)} \right]. \tag{2}$$

Here σ is the surface tension, and ρ, and μ the density and the viscosity with the subscripts 1 and 2 referring, respectively, to the gas and the liquid. P_2 is the total pressure (ambient and applied) far from the bubble and P_1 the pressure inside given by an equation of state for the gas. To first order in $a_n(t)$ an equation for the perturbation is derived which is presented here in the extended version including the effects of viscosity [18] with the boundary layer approximation [19,20]:

$$\ddot{a}_n(t) + B_n(t)\dot{a}_n(t) - A_n(t)a_n(t) = 0 \tag{3}$$

with

$$B_n(t) = \frac{3\dot{R}(t)}{R(t)} + \frac{2\mu_2}{[(n+1)\rho_1 + n\rho_2]\,R(t)^2} \times \left[-\beta + \frac{n^2(n+2)^2}{1 + 2\delta/R(t)} \right] \tag{4}$$

*levinsen@nbi.dk

and

$$A_n(t) = \frac{R(t)^2\ddot{R}(t)[(n+1)(n+2)\rho_1 - n(n-1)\rho_2] + \beta\sigma}{[(n+1)\rho_1 + n\rho_2]R(t)^3} + \frac{2\mu_2\dot{R}(t)}{[(n+1)\rho_1 + n\rho_2]R(t)^3}\left[\beta - \frac{n^2(n-1)(n+2)}{1+2\delta/R(t)}\right]. \tag{5}$$

Here $\beta = n(n-1)(n+1)(n+2)$, and δ represents the effective boundary layer where viscous effects are important:

$$\delta = \min\left(\delta_0\,[\mu/(\rho_2\,\omega)]^{1/2}, R(t)/(2n)\right). \tag{6}$$

The precise value of δ_0 to be used will be discussed later.

III. HIGHER ORDER EXPANSION

The present theory only tells when a shape distortion becomes unstable and no longer dies away but instead grows exponentially leading to bubble death. In order to look for possible saturation due to nonlinear effects at a level which might allow a stable distorted bubble to exist, the expansion here is taken a step further to second order.

The problem, as already noted by Plesset [17], in taking the expansion to higher order is that this mixes the different order spherical harmonics. During the derivation terms proportional to $Y_n^0(\theta,\phi)^2$ and $[\nabla Y_n^0(\theta,\phi)]^2$ appear. However, these terms can both be expressed in terms of sums involving spherical harmonics up to order $m = 2n$:

$$\sum_{i=1}^{2n} c_i Y_i^0(\theta,\phi), c_i = 0 \quad \text{for} \quad i \text{ odd}. \tag{7}$$

An important feature here is that only terms of even order appear regardless of whether n is even or odd.

As a first attempt this problem will be ignored and the derivation proceed as if terms are separable, with the mixing terms simply replaced by the relevant expansion term $c_n Y_n^0(\theta,\phi)$ corresponding to both upwards and downwards truncation. For $n = 2$ this poses no problem, but for $n = 3$ and higher an iterative process is needed, taking as a starting point this simpler derivation but with only upwards truncation.

A. Higher order expansion, separable

Using the aforementioned truncation the starting point for the derivation is still given by Eq. (1), although to ease keeping track of the order in the following $a_n(t)$ is replaced by $\epsilon\, a_n(t)$ with $0 < \epsilon =< 1$. Due to the truncation, this will still be the relevant surface even for the second order derivation.

The corresponding surface velocity is then

$$v(t) = \dot{R}(t) + \epsilon\dot{a}_n(t)Y_n^0(\theta,\phi). \tag{8}$$

The derivation closely follows that of Plesset [17] assuming that the velocity field can be described by a potential:

$$\Phi = \begin{cases} \Phi_1 = \left[R(t)^2\dot{R}(t)/r\right] - b_1 r^n Y_n^0(\theta,\phi) & r < R(t) \\ \Phi_2 = \left[R(t)^2\dot{R}(t)/r\right] - b_2 r^{-(n+1)} Y_n^0(\theta,\phi) & r > R(t) \end{cases}. \tag{9}$$

Equating $\nabla\Phi$ to $-v(t)$ at r_s, the unknown coefficients b_1 and b_2 are determined to second order in ϵ. Insertion in Φ then determines the potential to second order

$$\begin{aligned}\Phi_1 = {} & \frac{R(t)^2\dot{R}(t)}{r} - \frac{\epsilon r^n R(t)^{-n} Y_n^0(\theta,\phi)[2a_n(t)\dot{R}(t) + R(t)\dot{a}_n(t)]}{n} \\ & + \frac{\epsilon^2 r^n a_n(t) R(t)^{-n-1} Y_n^0(\theta,\phi)^2[(2n+1)a_n(t)\dot{R}(t) + (n-1)R(t)\dot{a}_n(t)]}{n}\end{aligned} \tag{10}$$

for the potential inside the bubble, and

$$\begin{aligned}\Phi_2 = {} & \frac{R(t)^2\dot{R}(t)}{r} + \frac{\epsilon r^{-n-1} R(t)^{n+1} Y_n^0(\theta,\phi)[2a_n(t)\dot{R}(t) + R(t)\dot{a}_n(t)]}{n+1} \\ & + \frac{\epsilon^2 r^{-n-1} a_n(t) R(t)^n Y_n^0(\theta,\phi)^2[(2n+1)a_n(t)\dot{R}(t) + (n+2)R(t)\dot{a}_n(t)]}{n+1}\end{aligned} \tag{11}$$

outside.

From the potentials the velocity fields can now be derived to second order by taking the gradient [$v(t) = -\nabla\Phi$]:

$$\mathbf{v_1(t)} = \begin{pmatrix} \frac{R(t)^2\dot{R}(t)}{r^2} \\ 0 \\ 0 \end{pmatrix} + \epsilon \begin{pmatrix} r^{n-1}R(t)^{-n}Y_n^0(\theta,\phi)[2a_n(t)\dot{R}(t) + R(t)\dot{a}_n(t)] \\ \frac{e^{-i\phi}r^{(n-1)}\sqrt{\Gamma(n+2)}R(t)^{-n}Y_n^1(\theta,\phi)[2a_n(t)\dot{R}(t)+R(t)\dot{a}_n(t)]}{n\sqrt{\Gamma(n)}} \\ 0 \end{pmatrix}$$
$$-\epsilon^2 \begin{pmatrix} r^{n-1}a_n(t)R(t)^{-n-1}Y_n^0(\theta,\phi)^2[(2n+1)a_n(t)\dot{R}(t) + (n-1)R(t)\dot{a}_n(t)] \\ \frac{2e^{-i\phi}r^{n-1}\sqrt{\Gamma(n+2)}a_n(t)R(t)^{-n-1}Y_n^0(\theta,\phi)Y_n^1(\theta,\phi)[(2n+1)a_n(t)\dot{R}(t)+(n-1)R(t)\dot{a}_n(t)]}{n\sqrt{\Gamma(n)}} \\ 0 \end{pmatrix}, \tag{12}$$

$$\mathbf{v_2(t)} = \begin{pmatrix} \frac{R(t)^2\dot{R}(t)}{r^2} \\ 0 \\ 0 \end{pmatrix} - \epsilon \begin{pmatrix} -r^{-n-2}R(t)^{n+1}Y_n^0(\theta,\phi)[2a_n(t)\dot{R}(t) + R(t)\dot{a}_n(t)] \\ \frac{e^{-i\phi}r^{-n-2}\sqrt{\Gamma(n+2)}R(t)^{n+1}Y_n^1(\theta,\phi)[2a_n(t)\dot{R}(t)+R(t)\dot{a}_n(t)]}{(n+1)\sqrt{\Gamma(n)}} \\ 0 \end{pmatrix}$$
$$+\epsilon^2 \begin{pmatrix} r^{-n-2}a_n(t)R(t)^nY_n^0(\theta,\phi)^2[(2n+1)a_n(t)\dot{R}(t) + (n+2)R(t)\dot{a}_n(t)] \\ -\frac{2e^{-i\phi}r^{-n-1}\sqrt{\Gamma(n+2)}a_n(t)R(t)^nY_n^0(\theta,\phi)Y_n^1(\theta,\phi)[(2n+1)a_n(t)\dot{R}(t)+(n+2)R(t)\dot{a}_n(t)]}{(n+1)\sqrt{\Gamma(n)}} \\ 0 \end{pmatrix}, \tag{13}$$

where $\Gamma(n) = (n-1)!$ is the gamma function.

Since the pressures at both sides of the bubble wall are to be calculated by the Bernoulli integral one needs to calculate $v(t)^2|_{r_s}$ to second order:

$$v_1(t)^2|_{r_s} = \dot{R}(t)^2 + 2\epsilon\dot{R}(t)\dot{a}_n(t)Y_n^0(\theta,\phi) + \epsilon^2\left\{\dot{a}_n(t)^2Y_n^0(\theta,\phi)^2 + \frac{e^{-2i\phi}\Gamma(n+2)Y_n^1(\theta,\phi)^2[2a_n(t)\dot{R}(t) + R(t)\dot{a}_n(t)]^2}{n^2\Gamma(n)R(t)^2}\right\}, \tag{14}$$

$$v_2(t)^2|_{r_s} = \dot{R}(t)^2 + 2\epsilon\dot{R}(t)\dot{a}_n(t)Y_n^0(\theta,\phi) + \epsilon^2\left\{\dot{a}_n(t)^2Y_n^0(\theta,\phi)^2 + \frac{e^{-2i\phi}\Gamma(n+2)Y_n^1(\theta,\phi)^2[2a_n(t)\dot{R}(t) + R(t)\dot{a}_n(t)]^2}{(n+1)^2\Gamma(n)R(t)^2}\right\}. \tag{15}$$

Furthermore the time derivatives of the potentials have to be evaluated at the bubble surface:

$$\frac{\partial\Phi_1}{\partial t} = R(t)\ddot{R}(t) + 2\dot{R}(t)^2 + \epsilon Y_n^0(\theta,\phi)\left\{\frac{-(n+2)a_n(t)\ddot{R}(t) + (n-3)\dot{R}(t)\dot{a}_n(t) - R(t)\ddot{a}_n(t)}{n}\right\}$$
$$+\epsilon^2 n^{-1}R(t)^{-2}Y_n^0(\theta,\phi)^2\big[(n+1)R(t)a_n(t)^2\ddot{R}(t) - (n+1)a_n(t)^2\dot{R}(t)^2$$
$$+2(n+1)R(t)a_n(t)\dot{R}(t)\dot{a}_n(t) + (n-1)R(t)^2\dot{a}_n(t)^2 - R(t)^2a_n(t)\ddot{a}_n(t)\big], \tag{16}$$

$$\frac{\partial\Phi_2}{\partial t} = R(t)\ddot{R}(t) + 2\dot{R}(t)^2 + \epsilon Y_n^0(\theta,\phi)\frac{[-(n-1)a_n(t)\ddot{R}(t) + (n+4)\dot{R}(t)\dot{a}_n(t) + R(t)\ddot{a}_n(t)]}{n+1}$$
$$+\epsilon^2(n+1)^{-1}R(t)^{-2}Y_n^0(\theta,\phi)^2\big[nR(t)a_n(t)^2\ddot{R}(t) - na_n(t)^2\dot{R}(t)^2$$
$$+2nR(t)a_n(t)\dot{R}(t)\dot{a}_n(t) + (n+2)R(t)^2\dot{a}_n(t)^2 + R(t)^2a_n(t)\ddot{a}_n(t)\big]. \tag{17}$$

The Bernoulli integral gives the pressures at either sides of the bubble wall

$$p_l = P_l + \rho_l\left[\left.\frac{\partial\Phi_l}{\partial t}\right|_{r_s} - \frac{1}{2}(\mathrm{grad}\Phi_l)^2|_{r_s}\right] \tag{18}$$

with $l = 1, 2$ with the difference $(p_1 - p_2)$ given by the surface tension term

$$\sigma\frac{2r + \epsilon n(n+1)a_n(t)Y_n^0(\theta,\phi)}{r^2}, \tag{19}$$

which to second order becomes

$$\sigma\frac{2R(t)^2 + \epsilon(n^2+n-2)R(t)a_n(t)Y_n^0(\theta,\phi) - 2\epsilon^2(n^2+n-1)a_n(t)^2Y_n^0(\theta,\phi)^2}{R(t)^3}. \tag{20}$$

The viscosity terms are much more difficult to treat due to their integro-differential nature. We have therefore only taken these to first order following the derivation of Prosperetti [18].

After addition of the viscous terms and subtraction of the zeroth order equation, the equation for $\ddot{a}_n$ can be written as

$$\ddot{a}_n(t) = -B_n(t)\dot{a}_n(t) + A_n(t)a_n(t) + C_n(a_n,\dot{a}_n,t), \tag{21}$$

where

$$\begin{aligned}C_n(a_n,\dot{a}_n,t) = [&2R(t)^2a_n(t)\dot{R}(t)\dot{a}_n(t)\{n^2\rho_2[(-2n^2+n+3)c_n\Gamma(n)+2d_n]+(n+1)^2\rho_1[n(2n+5)c_n\Gamma(n)-2d_n]\}\\&+2a_n(t)^2\{n(n+1)c_n[(2n^2+5n+3)\rho_1+(1-2n)n\rho_2]\Gamma(n)R(t)^2\ddot{R}(t)\}\\&-2a_n(t)^2\{[(n+1)^2\rho_1-n^2\rho_2]R(t)\dot{R}(t)^2[n(n+1)c_n\Gamma(n)+2d_n]+n^2(3n^2+3n-4)(n+1)^2\sigma c_n\Gamma(n)\}\\&+R(t)^3\dot{a}_n(t)^2(-(n^2\rho_2[(n^2+4n+3)c_n\Gamma(n)-d_n]+(n+1)^2\rho_1[d_n-(n-2)nc_n\Gamma(n)]))]/D_n(t)\end{aligned} \tag{22}$$

with

$$D_n(t) = [2n(n+1)((n+1)\rho_1+n\rho_2)\Gamma(n)R(t)^4]. \tag{23}$$

Here c_n and d_n specify the coefficients coming from the second order mixing terms, i.e., $Y_n^0(\theta,\phi)^2 \sim c_nY_n^0(\theta,\phi)$ and $e^{-2i\phi}\Gamma(n+2)Y_n^1(\theta,\phi)^2 \sim d_nY_n^0(\theta,\phi)$. Notice that no separation of terms in $a_n(t)$ and $\dot{a}_n(t)$ is possible now. Note also that the density ρ_1 of the gas is a time-dependent quantity while that of the liquid ρ_2 is considered constant. As expected, to first order Eq. (6) is reproduced.

The most likely perturbation to encounter is the ellipsoidal corresponding to $n = 2$:

$$\begin{aligned}C_2(a_2,\dot{a}_2,t) = c_2\{&8(9\rho_1+\rho_2)a_2(t)R(t)^2\dot{a}_2(t)\dot{R}(t)+4a_2(t)^2[3(7\rho_1-2\rho_2)R(t)^2\ddot{R}(t)+2(4\rho_2-9\rho_1)R(t)\dot{R}(t)^2+84\sigma]\\&-(9\rho_1+16\rho_2)R(t)^3\dot{a}_2(t)^2\}/[4(3\rho_1+2\rho_2)R(t)^4],\end{aligned} \tag{24}$$

where we have used that $d_2 = 3\,c_2$ and $c_2 = 2/7\,(5/4\pi)^{1/2}$.

Applying this correction we have simulated the behavior of an air bubble in the regime where measurements have shown stable shape distortion to occur.

B. Higher order expansion, interacting

The scheme laid out above works for the $n = 2$ case. However, for higher values of n a more intricate scheme has to be adopted. First, it is assumed that the nth spherical harmonic is excited and described by the result given above. Considering the surface of the kth harmonic

$$r_{sk}(t) = R(t) + a_k(t)Y_k^0(\theta,\phi), \tag{25}$$

with $k > n$, the velocity given by the nth harmonic is then treated as a perturbation:

$$v(t) = \dot{R}(t) + \eta\dot{a}_k(t)Y_k^0(\theta,\phi) + \epsilon\dot{a}_n(t)Y_n^0(\theta,\phi). \tag{26}$$

The velocity potentials for the kth surface are again given by Eq. (9) with k substituted for n. Treating the influence of the nth harmonic as a perturbation has the effect of separation of terms so the coupling terms can be calculated from the extra potentials

$$\delta\Phi = \begin{cases}\delta\Phi_1 = -b_1r^kY_k^0(\theta,\phi) & r < R(t)\\ \delta\Phi_2 = -b_2r^{-(k+1)}Y_k^0(\theta,\phi) & r > R(t)\end{cases} \tag{27}$$

by equating $\nabla\delta\Phi$ to $-\epsilon\dot{a}_n(t)Y_n^0(\theta,\phi)$ at r_{sk}. The unknown coefficients b_1 and b_2 are determined to first order in the product $\epsilon\eta$. Insertion in $\delta\Phi$ then determines the addition to the potentials coming from the perturbation:

$$\delta\Phi = \begin{cases}\delta\Phi_1 = \frac{(-1+k)r^k\epsilon\eta R(t)^{-k}Y_k^0(\theta,\phi)Y_n^0(\theta,\phi)a_k(t)\dot{a}_n(t)}{k} & r < R(t)\\ \delta\Phi_2 = \frac{(2+k)r^{-1-k}\epsilon\eta R(t)^{1+k}Y_k^0(\theta,\phi)Y_n^0(\theta,\phi)a_k(t)\dot{a}_n(t)}{1+k} & r > R(t)\end{cases}. \tag{28}$$

From the mixing part of the potentials, the mixing terms of the velocities can now be calculated as $\delta v(t) = -\nabla(\delta\Phi)$. As $\delta v(t)$ already is first order in the product $\epsilon\,\eta$, the only new terms in $v(t)^2$ to appear come from the products $v_0\,\delta v(t)$ with $v_0 = R(t)^2\dot{R}(t)/r^2$ the velocity of the undisturbed spherical surface:

$$\delta v(t)^2|_{r_s} = \begin{cases}\delta v_1(t)^2|_{r_s} = -2(-1+k)\epsilon\eta Y_k^0(\theta,\phi)Y_n^0(\theta,\phi)a_k(t)\dot{R}(t)\dot{a}_n(t)/R(t) & r < R(t)\\ \delta v_2(t)^2|_{r_s} = 2(2+k)\epsilon\eta Y_k^0(\theta,\phi)Y_n^0(\theta,\phi)a_k(t)\dot{R}(t)\dot{a}_n(t)/R(t) & r > R(t)\end{cases}. \tag{29}$$

Now one needs to calculate the corrections to the time derivatives of the potentials at the surface r_{sk}, which to first order in the product $\epsilon\,\eta$ becomes

$$\frac{\partial\delta\Phi_1}{\partial t} = -\frac{(-1+k)\epsilon\eta Y_kY_n\{-R(t)\dot{a}_k(t)\dot{a}_n(t)+a_k(t)(k\dot{R}(t)\dot{a}_n(t)-R(t)\ddot{a}_n(t))\}}{kR(t)}, \tag{30}$$

$$\frac{\partial\delta\Phi_2}{\partial t} = \frac{(2+k)\epsilon\eta Y_kY_n(R(t)\dot{a}_k(t)\dot{a}_n(t)+a_k(t)((1+k)\dot{R}(t)\dot{a}_n(t)+R(t)\ddot{a}_n(t)))}{(1+k)R(t)}. \tag{31}$$

The final step is to calculate the extra term coming from the surface tension. As the interaction here is mediated directly by the distortion of the surface, one has to consider the combined distortion,

$$r_{skn}(t) = R(t) + \eta a_k(t) Y_k^0(\theta,\phi) + \epsilon a_n(t) Y_n^0(\theta,\phi), \tag{32}$$

giving

$$\sigma \frac{2r + \eta k(k+1) a_k(t) Y_k^0(\theta,\phi) + \epsilon n(n+1) a_n(t) Y_n^0(\theta,\phi)}{r^2}. \tag{33}$$

Evaluating this at the surface $r_{skn}(t)$ one finds the mixing term

$$-\sigma \frac{2(-2+k+k^2+n+n^2)\epsilon\eta Y_k^0(\theta,\phi) Y_n^0(\theta,\phi) a_k(t) a_n(t)}{R(t)^3}. \tag{34}$$

Adding the above terms to the relevant Bernoulli integrals and the surface term for the kth mode, one can find the correction $\delta\ddot{a}_k(t)$ to $\ddot{a}_k(t)$,

$$\begin{aligned}\delta\ddot{a}_k(t) = [&R(t)^3[(-1+k^2)\rho_1 - k(2+k)\rho_2]\dot{a}_k(t)\dot{a}_n(t) + a_k(t)(2k(1+k)(-2+k+k^2+n+n^2)\sigma a_n(t)) \\ &+(R(t)^2\{(k(2+k)\rho_2((1+k)\dot{R}(t)\dot{a}_n(t) - R(t)\ddot{a}_n(t)) + (-1+k^2)\rho_1(k\dot{R}(t)\dot{a}_n(t) + R(t)\ddot{a}_n(t))\})]D_{nk}\end{aligned} \tag{35}$$

with

$$D_{nk} = c_{nk}\epsilon/\{R(t)^4[(1+k)\rho_1 + k\rho_2]\} \tag{36}$$

and c_{nk} the coefficient of $Y_k^0(\theta,\phi)$ in the expansion of the product $Y_n^0(\theta,\phi)Y_k^0(\theta,\phi)$.

This has the advantage of being independent of whether modes are even or odd. For $k = 3$ a term is added due to the interaction with the lower $n = 2$ distortion. For $k = 4$ interaction with both $n = 2$ and $n = 3$ is possible. As the interactions are treated as perturbations, the corrections are calculated independently using the result derived above. However, for modes $n = 2$, 3, and 4 in the interval so far investigated ($c = 0.0005$–0.00385) the $n = 2$ mode becomes unstable before the other modes are even excited!

IV. SIMULATIONS

In this section the model used for the simulation of the undisturbed spherical oscillation will be discussed before the results of the actual simulation will be presented.

A. Model for spherical oscillation

As a starting point for the simulations is chosen the form of the Rayleigh-Plesset (RP) equation introduced by Löfstedt *et al.* [21], where the dynamics of the bubble wall $R(t)$ is described by

$$\begin{aligned}R\ddot{R} + \frac{3}{2}\dot{R}^2 = &\frac{1}{\rho}\{P_g[R(t)] - P_f(t) - P_0\} \\ &+\frac{R}{\rho c}\frac{d}{dt}\{P_g[R(t)] - P_f(t)\} - 4\nu\frac{\dot{R}}{R} - \frac{2\sigma}{\rho R}.\end{aligned} \tag{37}$$

Here P_g is the uniform gas pressure inside the bubble, $P_f = -P_a \sin(\omega t)$ is the forcing pressure with angular frequency ω, P_0 is the ambient pressure during the measurements, and the remaining parameters are material constants of the host liquid, e.g., c is the speed of sound, ρ its density, and ν is the kinematic viscosity. In the following some more details are presented even though all can be found in, e.g., Ref. [2].

The gas pressure P_g is related to $R(t)$ through an equation of state. A polytropic van der Waals equation of state is used, modified to include the effects of surface tension σ [22]:

$$P_g[R(t)] = \left(P_0 + \frac{2\sigma}{R_0}\right)\frac{\left(R_0^3 - a^3\right)^\gamma}{[R(t)^3 - a^3]^\gamma}. \tag{38}$$

Here a is the hard core van der Waals radius of the gas (for argon $a = R_0/8.86$). The polytropic exponent γ is set to change between 1 for most of the cycle increasing toward a weighted average for argon and water vapor, according to the instantaneous Péclet number [23], $\mathrm{Pe} = R_0^2|\dot{R}(t)|/R(t)\kappa$, with κ being the thermal diffusivity of the gas.

The connection between γ and the Péclet number has been tabulated by Prosperetti [23] although we use the simple fit given by Hilgenfeldt *et al.* [24]. Since γ now depends on $\dot{R}(t)$, the situation reverts to isothermal around the immediate time of the collapse. Various methods have been devised to circumvent the problem, but here this aspect has simply been ignored following Ref. [24].

The effect of water vapor (evaporation and condensation) is included by assuming a simple Hertz-Knudsen model for the change of moles during a cycle [25]:

$$\begin{aligned}\dot{N}_{H_2O} &= \dot{N}_{\mathrm{H_2O}}^{\mathrm{evap}} - \dot{N}_{\mathrm{H_2O}}^{\mathrm{cond}} \\ &= \frac{4\pi R^2\alpha}{M_{\mathrm{H_2O}}}\frac{\bar{c}(T_s)}{4}\left[\rho_{g,\mathrm{H_2O}}^{\mathrm{sat}} - \rho_{g,\mathrm{H_2O}}(t)\right],\end{aligned} \tag{39}$$

where α is the accommodation coefficient. The commonly accepted value is 0.4; see, however, Refs. [26,27].

$M_{\mathrm{H_2O}}$ is the molar mass of water, and $\bar{c}(T_s) = \sqrt{8R_{\mathrm{gas}}T_s/(\pi M_{\mathrm{H_2O}})}$ the average velocity of water molecules at the inside wall of the bubble with the temperature T_s locally assumed to be given by the ambient temperature T_0. $\rho_{g,\mathrm{H_2O}}^{\mathrm{sat}}$ and $\rho_{g,\mathrm{H_2O}}(t)$ are, respectively, the saturated vapor density and the time-dependent average vapor density in the bubble. Finally the stable bubble size is determined using diffusive stability.

B. The (P_a, R_0) parameter space

In the following some representative examples of the simulations performed on the models described above are presented. The simplified model used for the basic spherical

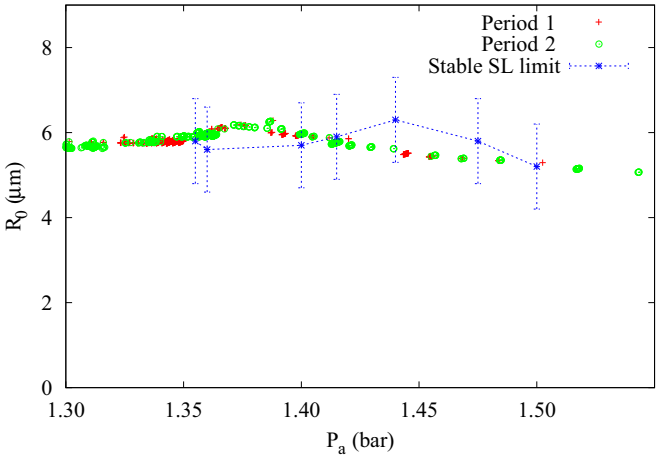

FIG. 1. (Color online) Result of simulation showing locations of stable period 1 and period 2 shape distortion in the rest radius R_0, drive pressure P_a parameter space. Also shown are data for the highest possible stable sonoluminescing state taken from Simon *et al.* [28].

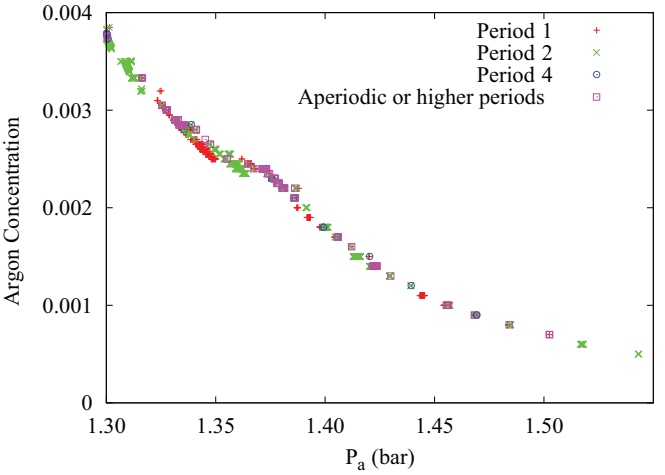

FIG. 2. (Color online) Locations of stable period shape distortion in the argon concentration, drive pressure P_a parameter space from Fig. 1 but also with regions of higher order and seemingly aperiodic modes filled in.

oscillation that drives the instabilities was chosen in order to limit the computing time. This has some repercussions that will be commented on where the simulations are compared to actual measurements. Unless otherwise noted, the simulations are done for a temperature of 6 °C using for the surface tension and viscosity the values of clean water. The frequency of the drive is 22 kHz, and the accommodation constant is 0.4. In these runs the prefactor δ_0 in the effective boundary layer is set to 0.3. First, the simulation is run without invoking the shape instability. After a stable undisturbed bubble cycle has been established, the calculation proceeds for 160 cycles or more in order to determine whether a possible excited shape distortion is stable and ensure that enough cycles are present to establish the period. In this phase the $n = 2$, 3, and 4 shape distortions are investigated. However, the $n = 3$ and 4 modes have never been seen to be excited before the $n = 2$ shape distortion becomes unstable!

First, a illustrative scan over some of the P_a, R_0 parameter space is presented showing areas of stable period 1 and period 2 shape oscillations compared with measurements showing the experimental limit for stable SBSL determined by Simon *et al.* [28] (see Fig. 1). A reasonable agreement is seen, although one should bear in mind that the experimental determination of R_0 and P_a is based on fits to a specific model of SBSL using the relative timing of the sonoluminescent emission.

The same data are plotted in Fig. 2 but now in the parameter space of argon concentration versus P_a. Also shown are regions of higher period modes and seemingly aperiodic modes. We have observed period 3, 4, 5, 6, and 8 modes, but only the period 4 mode is plotted individually in the figure; the rest are lumped together in higher order modes as their occurrences are rare. Some of the modes labeled aperiodic may actually be higher order modes but without enough cycles calculated for positive identification. Finally, bursting or intermittent modes have been observed so probably chaotic modes are also present in the system. One should bear in mind, though, that other mechanisms might limit the experimentally accessible parameter space both at the high and the low end of the concentration range.

Next, the diffusive stability curve in the P_a, R_0 parameter space is plotted for an argon concentration of 0.00255 showing regions of period 1 and period 2 stable shape distortion (see Fig. 3). Notice the gap in the period 2 section where no stable solutions are found to exist. This agrees with experimental observations [7] and with the studies of Holzfuss [29] on shape instabilities. The arrows show the operating points of the next figures where stable periods 1 and 2 are displayed.

The middle panel of Fig. 4 demonstrates the growth and saturation of a period 2 cycle at a drive pressure corresponding to the arrow to the right pointing to the blue (x) section in Fig. 3 for an otherwise stable bubble oscillation as shown in the upper panel, with an amplified view in the lower panel. An expanded view is shown in the two upper panels of Fig. 5, with an amplified view also showing the period doubling of

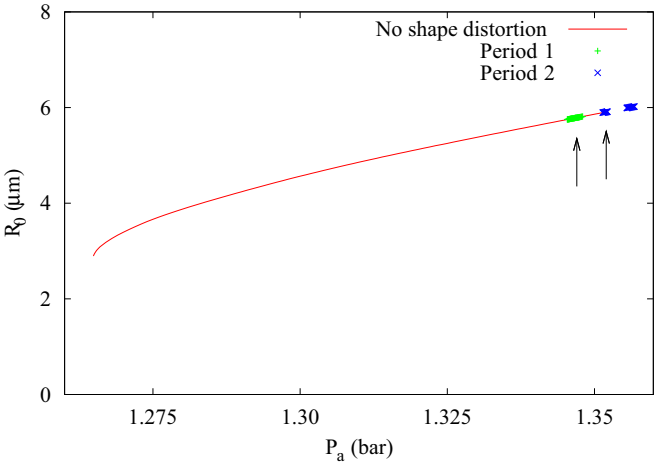

FIG. 3. (Color online) Simulated rest radius R_0 versus drive pressure P_a for an air bubble with relative argon concentration 0.00255. In the green section (+) stable period 1 shape distortion is present. Stable period 2 shape distortion is present in the blue (x) sections. No stable solutions are found in between. The arrows show the operating points for the next figures.

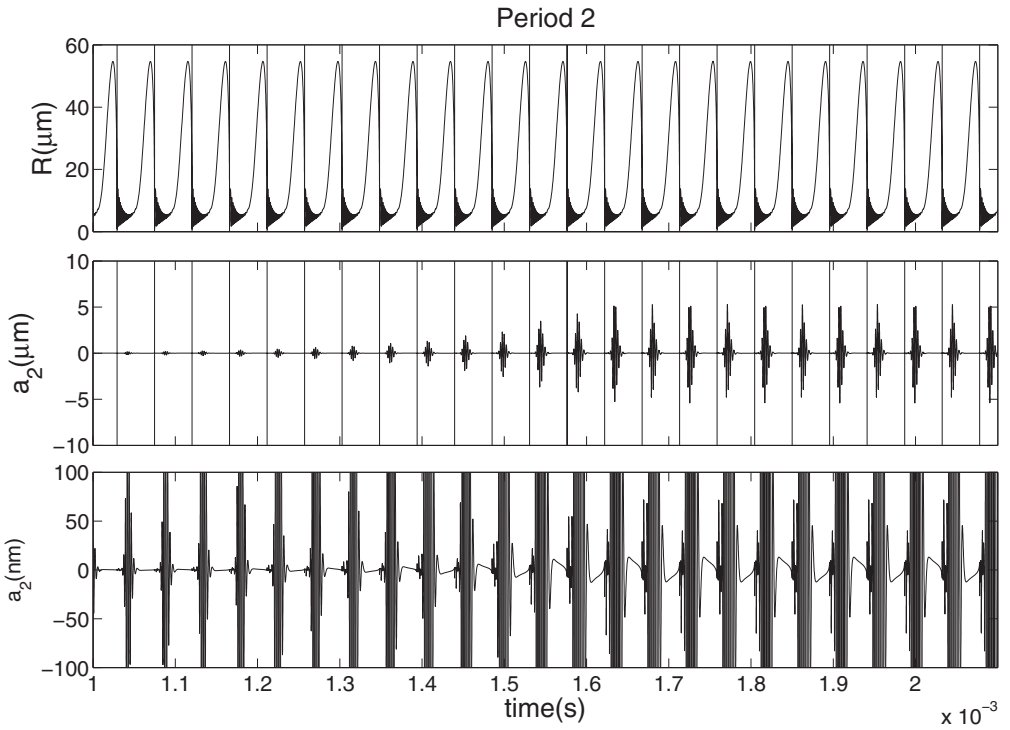

FIG. 4. Upper panel: The undisturbed bubble oscillation. Middle panel (scale μm): Growth and saturation of the excited period 2 shape distortion a_2 computed at the arrow pointing to the blue section in Fig. 3. The vertical lines show the timing of the main collapse. Lower panel (scale nm): Magnified view of a_2.

the stabilized Rayleigh-Taylor instability at the main collapse, which could be related to the observations of period doubling in the emitted light [5–7]. The shape oscillation saturates at a level just before the bubble would probably break as a ratio of one is normally taken as the criterion for bubble death. This is demonstrated in the lowest panel where the ratio between the

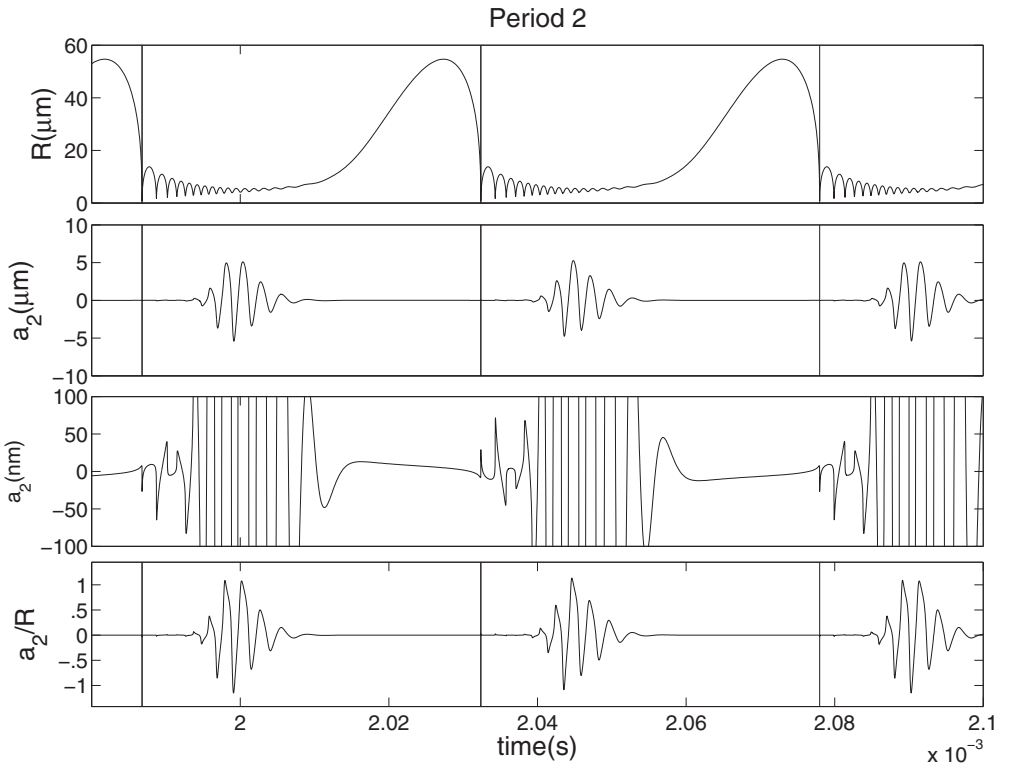

FIG. 5. Expanded view of the saturation part of the excited period 2 shape distortion shown in Fig. 4. Both Rayleigh-Taylor (the first sharp peaks) and later after-bounce shape oscillations are present.

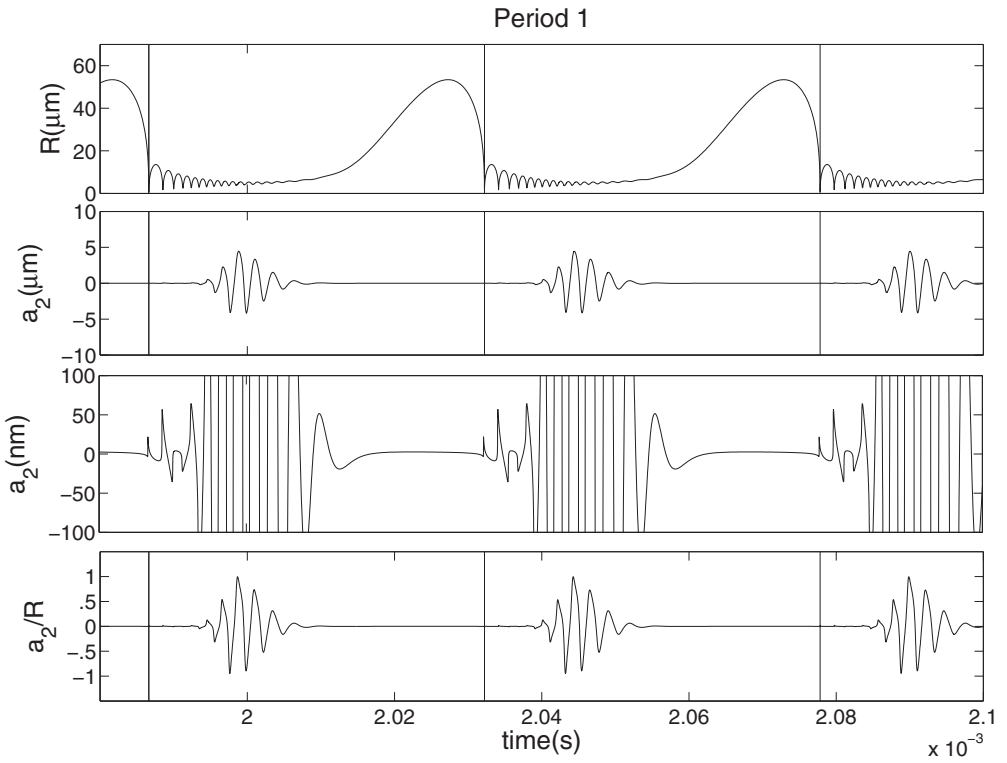

FIG. 6. Saturation of the excited period 1 shape distortion computed at the arrow pointing to the green section in Fig. 3.

shape oscillation a_2 and the instantaneous bubble radius $R(t)$ is displayed, thus explaining why the period doubled states are found just below or even in stable islands beyond the critical line for bubble death. Again it might mean that not all states found are necessarily experimentally accessible.

Finally in Fig. 6 a saturated period 1 cycle corresponding to the arrow pointing at the green (+) section in Fig. 3 is displayed. From top to bottom the panels show the undisturbed bubble oscillation $R(t)$, the saturated shape oscillation a_2, a magnified view of a_2 displaying the Rayleigh-Taylor excitation, and the ratio $a_2/R(t)$, which again is close to unity where bubble death is expected.

C. Influence of δ_0

Over the years various authors have suggested different values of the constant δ_0 in the boundary layer approximation to be used in order to explain experimental observations of the extinction boundary. Values ranging from the original value of unity [19,20], over, e.g., 1/3 [30], 1/4 [30], to zero [29,31] have thus been proposed. In the overview of the (P_a, R_0) parameter space given above the value 0.3 was used for δ_0. Keeping all other parameters as before the influence of δ_0 will now be investigated. In Fig. 7 the result is presented. This figure should be compared to Fig. 3 as the positions of the period 1 (denoted P1) and period 2 (denoted P2) shape distortions follow the same (P_a, R_0) curve of diffusional stability.

As seen, the positions of the distortions move toward higher values of R_0 (and P_a), and the order of P1 and P2 is even exchanged as the value of the parameter δ_0 decreases. At the same time the size of the R-T peak at the main collapse grows from about 2% at $\delta_0 = 1$ to about 10% at $\delta_0 = 0$, suggesting that excitation and saturation of the R-T instability could be behind the observation of period doubling in the emission. Furthermore, that a value of δ_0 close to zero is in fact most likely.

Following this lead a comparison is now made with the period doubled emission reported by Ref. [7]. Here stable period doubled emission was found in a rather large interval of forcing pressure P_a for an air bubble ($T = 9\,^{\circ}$C) at a

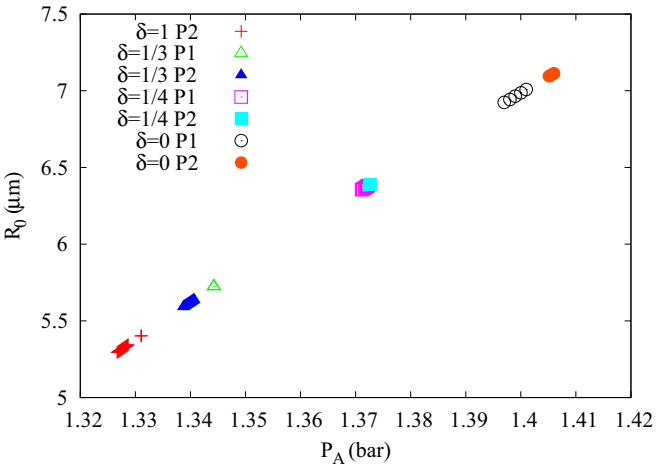

FIG. 7. (Color online) Position along the diffusional stability curve of Fig. 3 of the period 1 (denoted P1) and period 2 (denoted P2) shape distortions as function of the parameter δ_0. Notice that as δ_0 goes to zero the position proceed to higher values of R_0 (and P_a) and the order of P1 and P2 is exchanged.

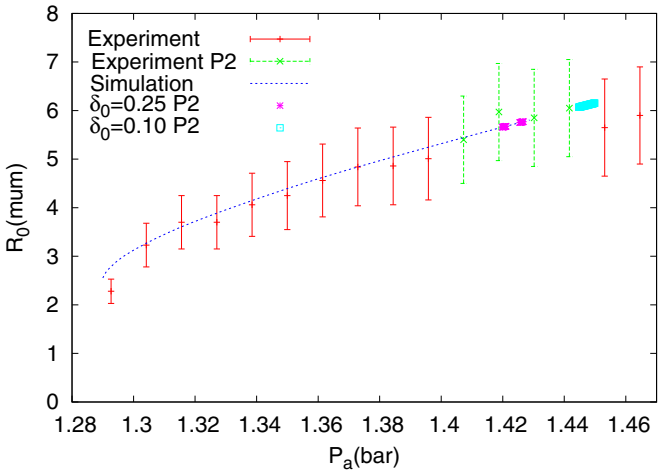

FIG. 8. (Color online) Experimental data showing the position of period doubled emission in P_a, R_0 parameter space from a sonoluminescing bubble (data from Ref. [7]), compared to simulation with input values $\delta_0 = 0.25$ and $\delta_0 = 0.1$.

corresponding argon concentration of 0.00135. A simulation with these parameters has been performed for $\delta_0 = 0.25$ and 0.1 and compared with the experimental data in Fig. 8. $\delta_0 = 0.25$ seems to be in best accordance with the experiment with $a_2/R = \pm$ 2% at the time of the major collapse, while that of $\delta_0 = 0.1$ is about $\pm$4%. In order to compare to the experiment some details about the models involved need to be discussed.

The experimental (P_a, R_0) data are obtained from fits to a model that is somewhat different from the present one; for instance, the boundary for extinction is computed with the thickness of the boundary layer is set to zero, and the amount of water vapor is kept constant, so one would not expect a perfect overall agreement. In the experiment R_0 and the corresponding value of the driving pressure P_a was estimated from the relative timing of the collapse (see Refs. [28,33]) since the set up did not allow for a simultaneous Mie scattering experiment. The pressure axis was scaled linearly such that the onset of light emission in the experiment, which of course has some inherent uncertainty associated, corresponded to the onset of the diffusional stability curve of the simulation. As the value of the onset pressure will be model dependent, in the present comparison the experimental value of the pressure has simply been rescaled to fit the present model. Due to the rather large uncertainty in the values of R_0 it has not been deemed necessary to recalibrate this quantity.

Overall the agreement is satisfying with the most striking difference being that the simulation gives a smaller interval where period doubling of the emission could be expected. This could be caused by some of the experimental data being from increasingly less stable islands beyond the border of extinction that was missed in the simulation. Such an island is actually seen in the simulation for $\delta_0 = 0.25$ together with high order and aperiodic solutions. These latter are not shown in the figure for clarity but due to noise a period 4 realization may accidentally be mistaken for a period 2 in the experiment. Another possibility, more likely perhaps, is that the model for the radial oscillation that is giving the input to the computation of the distortion is not treating the behavior correctly close to the main collapse [2]. Apart from the model dependence already discussed, the estimate solely relies on the determination of the argon concentration, which may be underestimated since the experiment was performed in a semiopen cell. Also, due to the absence of a direct measurement of the bubble oscillation it is not known whether any shape distortion was present.

Finally, whether the computed deviation from the spherical shape is large enough to give rise to the observed period doubling is naturally of interest. Unfortunately very little information is available touching on this question. In Ref. [34] the far field emitted light intensity is calculated for a ellipsoidal bubble with major axis $a = 1$ μm and minor axes $b = 0.750$ μm compared to approximately $a = 850$ nm and $b = 800$ nm in the simulation above. The emission is approximated as coming from a point source at the center of the bubble. The calculation is based on diffraction of the electric field vector in the bubble surface and the refractive index of the water is 1.33, while that of the gas in the bubble is assumed to be 1. For a center wavelength between 250 and 450 nm the peak to peak (pk-pk) value of the intensity variation is about 40–50%. To find the period doubling the intensity difference between the emission from a prolate and an oblate spheroid of identical volumes is needed. To first order this is, however, expected to be of the order of the angular variation for the prolate spheroid. Assuming for simplicity a linear dependence for the intensity on the distortion a pk-pk period doubling of approximately 10% should be expected compared to the actually 16% observed in Ref. [7]. Dam [35] considered a model based on Kirchhoff's diffraction formula [36] together with the assumption of volume emission from a central spherical region. Using a bubble size of $a = 1.1$ and $b = 1$ μm together with the same refractive index of water as Madrazo *et al.* but with that of the gas set to 1.125, the author found a pk-pk angular intensity variation of 10% for a Gaussian wavelength distribution around 350 nm with a FWHM of 70 nm. The radius of the central region was changed from 0.1 to 0.7 μm without any appreciable change in the intensity distribution. Scaling the wavelength with the bubble size again suggests a pk-pk period doubling of 6–8% from the distortion calculated in the simulation above at a center wavelength of 270 nm. Taking the somewhat shaky assumptions used in the models into account, while not conclusive, this analysis does show that excitation of the Rayleigh-Taylor mode is indeed a strong candidate to be the cause of the experimentally observed period doubling.

V. DISCUSSION

In the previous sections the theory of shape distorted bubble oscillations have been extended to show that saturation of these modes are indeed possible. This explains nicely the recent observation using Mie scattering [11] of stable period doubled structures in the after-bounce region of the radial bubble oscillation of a sonoluminescing bubble [12]. Also earlier experiments showing period doubling of the emitted light [5–7] seem explainable by this mechanism as suggested by Holzfuss [29]. However, there are still some unresolved issues. The structures seen in the simulations come too late

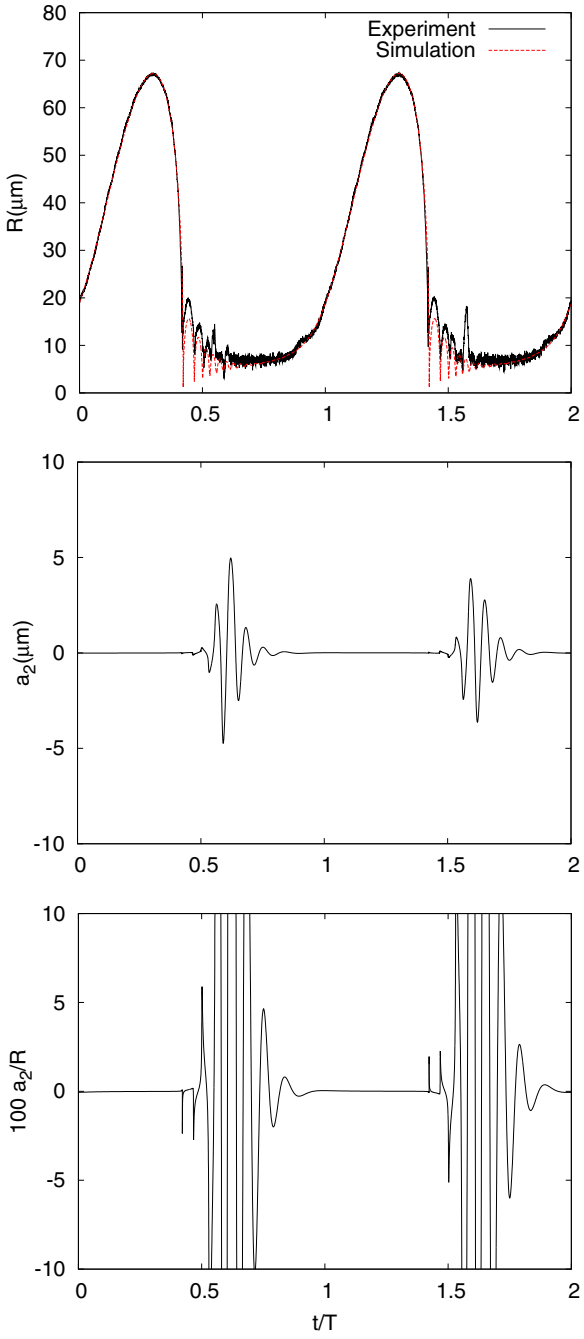

FIG. 9. (Color online) Mie scattering [12] from a sonoluminescing bubble ($c \sim 0.25$, $T = 9°$) that simultaneously exhibits period double emission compared to simulation with input values $\mu_{\text{eff}} = 4\mu$, $\alpha = 0.25$ used for the simulation of $R(t)$ while μ is used in the simulation of a_2 together with $\delta = 0.3$. Experimental data are time averaged over 20 consecutive sets, each lasting four periods to accentuate the period doubling of the structures in the after-bounce regions.

in the after-bounce region and the size of the Rayleigh-Taylor instability at the main collapse is somewhat small to be able to explain the period doubling of the light. Both of these problems may, however, be connected to the specific version of the Rayleigh-Plesset equation used to simulate the radial bubble oscillation, which has the after bounces fall off too slowly. The present version was chosen in order to cut down on computer time. Since the radial oscillation serves as input to the computation of the shape distortion, one way around this problem, which does not involve spending more computer time, is to change the value of some of the constants used for either the surface tension, viscosity (see Ref. [32]), or accommodation constant (see Refs. [26,27]) in order to mimic the radial oscillation while keeping the correct values in the computation of the shape instability.

In the following simulations of $R(t)$ the accommodation constant has been changed to $\alpha = 0.25$ as suggested by Ref. [26] and the viscosity has been multiplied by four [32]. In the simulation of a_2 the value of the prefactor δ_0 is set to 0.3, in order to find a period-doubled disturbance close to the value of 0.250 suggested above. As seen from Fig. 9 (upper panel), this has the sought for effect of making the after bounces fall off faster. Also it can be seen from comparing the upper and the middle panel that the structures in a_2 now agree reasonably well with the structures actually observed for a sonoluminescing bubble [12]. The measurement was performed on an air bubble at 9°C with a relative argon concentration of approximately 0.0025. The fit from the upper panel gives $R_0 = 7.33\,\mu$m. Concomitant with the measurement of the structures were observed period doubling in the emission. The lower panel gives a magnified view of a_2/R showing that the distortion of the Rayleigh-Taylor instability at the time of the main collapse is still only a few percent though. To ease the comparison, the upper panel displays the experimental $R(t)$ trace compared to the simulated. There is of course no reason to believe that this gives a truly realistic picture of the Mie scattering signal since that is a result of interference of monochromatic light scattered from different points on the surface of the bubble. Also the direction in space of the symmetry axis of the bubble distortion is unknown. However, it is reasonable to expect any structures to be at least situated correctly in time.

While the above of course can be considered proof of concept, simulations on a model that better capture the basic features of the undistorted radial oscillation of the bubble are needed before the question of the connection between bubble distortion and the spatially anisotropic emission can finally be considered settled.

VI. CONCLUSION

Extending the theory for shape oscillations to second order shows that saturation is possible in the regime where stable shape oscillations are seen experimentally. Due to the integro-diffential nature of the viscous terms, these are, however, still included only to first order. One feature that does fit the experimental observations is that the rise of the shape distortion to its maximal value seems to be rather abrupt. The size of the R-T shape distortion at the time of the emission is of order 20–100 nm (corresponding to ±2–10% of the minimum bubble radius) depending especially on the thickness of the viscous boundary layer. According to calculations by Dam [35] this is just enough to produce visible period doubling as seen in the emission. The result of that analysis is, however, very dependent on parameters such as the size of the effectively emitting volume and the refractive

index inside the bubble close to the surface, about which there is precious little information [4,37]. So it seems that the R-T shape distortion could be the cause for the spatially anisotropic period doubling seen in the emission, while the after-bounce-driven shape distortion shows up in the Mie scattering. Both are then stabilized by the parametric shape distortion driven by the drive signal.

The possible application of the present analysis to encapsulated bubbles used for medical purposes such as contrast agents and for precise localized medication could be of practical interest (see, e.g., Refs. [13–15]). Finally, saturation may also be of interest in the field of inertial confinement fusion (see, e.g., Ref. [16]).

ACKNOWLEDGMENTS

The author thanks K. Musztacs for help with preparation and experimental data analysis and A. Prosperetti and B. Lautrup for illuminating discussions. The author acknowledges financial support from the Danish National Science Foundation and Brødrene Hartmanns Fond.

[1] D. F. Gaitan, L. A. Crum, R. A. Roy, and C. C. Church, J. Acoust. Soc. Am. **91**, 3166 (1992).
[2] M. P. Brenner, S. Hilgenfeldt, and D. Lohse, Rev. Mod. Phys. **74**, 425 (2002).
[3] W. Lauterborn and T. Kurz, Rep. Prog. Phys. **73**, 106501 (2010).
[4] K. Weninger, S. J. Putterman, and B. P. Barber, Phys. Rev. E **54**, R2205 (1996).
[5] J. S. Dam, M. T. Levinsen, and M. Skogstad, Phys. Rev. Lett. **89**, 084303 (2002).
[6] J. S. Dam, M. T. Levinsen, and M. Skogstad, Phys. Rev. E **67**, 026303 (2003).
[7] M. T. Levinsen, N. Weppenaar, J. S. Dam, G. Simon, and M. Skogstad, Phys. Rev. E **68**, 035303 (2003).
[8] J. A. Ketterling and R. E. Apfel, Phys. Rev. E **61**, 3832 (2000).
[9] R. G. Holt and D. F. Gaitan, Phys. Rev. Lett. **77**, 3791 (1996).
[10] H. Lin, B. D. Storey, and A. J. Szeri, Phys. Fluids **14**, 2925 (2002).
[11] G. Mie, Ann. Phys. **330**, 377 (1908).
[12] M. T. Levinsen, Ultrasonics **54**, 637 (2014).
[13] D. L. Miller, S. V. Pislaru, and J. F. Greenleaf, Somat. Cell Mol. Genet. **27**, 115 (2002).
[14] K. Ferrara, R. Pollard, and M. Borden, Annu. Rev. Biomed. **9**, 415 (2007).
[15] R. Rao and S. Nanda, JPP **61**, 689 (2009).
[16] S. Pfalzner, *An Introduction to Inertial Confinement Fusion* (Taylor & Francis, Philadelphia, 2006).
[17] M. S. Plesset, J. Appl. Phys. **25**, 96 (1954).
[18] A. Prosperetti, Quart. Appl. Math. **34**, 339 (1977).
[19] A. Prosperetti, Acc. Nazionale dei Lincei, Rendiconti della Classe de Scienze Fisiche, Matematiche e Naturali Ser. 8 **62**, 196 (1977).
[20] M. P. Brenner, D. Lohse, and T. F. Dupont, Phys. Rev. Lett. **75**, 954 (1995).
[21] R. Löfstedt, K. Weninger, S. Putterman, and B. P. Barber, Phys. Rev. E **51**, 4400 (1995).
[22] A. Prosperetti, L. A. Crum, and K. W. Commander, J. Acoust. Soc. Am. **83**, 502 (1988).
[23] A. Prosperetti, J. Acoust. Soc. Am. **61**, 17 (1977).
[24] S. Hilgenfeldt, S. Grossmann, and D. Lohse, Phys. Fluids **11**, 1318 (1999).
[25] K. Yasui, J. Phys. Soc. Jpn. **66**, 2911 (1997).
[26] G. F. Puente and F. J. Bonetto, Phys. Rev. E **71**, 056309 (2005).
[27] J. Holzfuss and M. T. Levinsen, Phys. Rev. E **77**, 046304 (2008).
[28] G. Simon, I. Csabai, A. Horvath, and F. Szalai, Phys. Rev. E **63**, 026301 (2001).
[29] J. Holzfuss, Phys. Rev. E **77**, 066309 (2008).
[30] Y. An, T. Lu, and B. Yang, Phys. Rev. E **71**, 026310 (2005).
[31] L. Yuan, C. Y. Ho, M.-C. Chu, and P. T. Leung, Phys. Rev. E **64**, 016317 (2001).
[32] B. P. Barber, R. A. Hiller, R. Löfstedt, S. J. Putterman, and K. R. Weninger, Phys. Rep. **281**, 65 (1997).
[33] G. Simon and M. T. Levinsen, Phys. Rev. E **67**, 026320 (2003).
[34] A. Madrazo, N. García, and M. Nieto-Vesperinas, Phys. Rev. Lett. **80**, 4590 (1998).
[35] J. S. Dam, Ph.D. thesis, Niels Bohr Institute, University of Copenhagen, 2006.
[36] R. W. Ditchburn, *Light* (Academic Press, London, 1976).
[37] J. S. Dam and M. T. Levinsen, Phys. Rev. Lett. **92**, 144301 (2004).